

Cite this: *J. Mater. Chem. A*, 2020, **8**, 5062Received 15th November 2019
Accepted 16th February 2020

DOI: 10.1039/c9ta12573f

rsc.li/materials-a

Fast production of zinc–hexamethylenetetramine complex microflowers as an advanced sulfur reservoir for high-performance lithium–sulfur batteries†

Xiaoyuan Dou,^{‡a} Gaoran Li,^{‡a} Wenyao Zhang,^a Fei Lu,^{ab} Dan Luo,^{IDa} Wenwen Liu,^a Aiping Yu^{ID*^a} and Zhongwei Chen^{ID*^a}

A unique zinc–hexamethylenetetramine coordination complex (ZnHMT) has been developed through a facile and fast solution-based method. The ZnHMT complex delivers an exquisite flower-like nano-architecture assembled by ultrathin nanosheets, which not only facilitates the electrolyte infiltration and ion transfer, but also implements efficient exposure of active interfaces. Meanwhile, the strong chemical interactions between ZnHMT and polysulfides render potent sulfur immobilizations, contributing to effective inhibition of the shuttling behavior. As a result, Li–S cells with a ZnHMT-based interlayer achieve excellent cyclability over 1000 cycles, superb rate capability up to 5C and a high areal capacity of 5.9 mA h cm⁻² under raised sulfur loading.

Despite the tremendous commercial success of lithium-ion batteries in portable electronics, the pursuit of more powerful battery technology has never ceased to meet the rapid development of extended applications, such as electrical vehicles and grid-scale energy storage.^{1–4} Under such circumstances, lithium–sulfur (Li–S) batteries are drawing increasing attention due to their intriguingly high energy density (2600 W h kg⁻¹) and cost effectiveness.^{5,6} However, the state-of-the-art Li–S batteries are still suffering from several major obstructions to their practical implementations. Most representatively, the intermediate lithium polysulfides (LiPSs) readily dissolve in the electrolyte and freely migrate between the anode and cathode regions. This behavior, known as the “shuttle effect”, induces irreversible sulfur consumption, anode passivation and coulombic inefficiency, resulting in an unstable and inefficient battery chemistry.^{7–10} Moreover, the poor conductivity of both

sulfur and its lithiation products, as well as the large volume variation upon the lithiation–delithiation process, causes serious electrochemical polarizations and greatly limits the sulfur utilization and rate capability.^{11–13}

Targeting these challenges, rational interlayer designs have been exploited with great potential in regulating the shuttling behavior for stabilized sulfur electrochemistry. Well-selected interlayer materials are expected to establish a secondary barrier against LiPS permeation through the separator, which is compatible and collaborative with the widely-reported cathode strategies towards substantial enhancements in sulfur utilization and shuttle suppression.^{14–17} In this regard, promising outcomes have been accomplished by applying various carbons, polar inorganics, and their composites as interlayer candidates based on their physical or/and chemical LiPS confinements.^{18–22} Recently, metal–organic frameworks (MOFs) have been emerging as a promising alternative for the construction of advanced interlayers in Li–S batteries. Attributed to the ordered coordination between the metal nodes and organic ligands, MOF materials are endowed with extensive crystalline, architectural and surface chemical features for a broad range of applications.^{23,24} In the scenario of Li–S batteries, the highly porous MOFs could benefit the spatial confinement of sulfur species, while the open metal sites and polar organic ligands could implement highly favorable interactions with LiPSs toward effective chemical sulfur immobilization.^{25,26} However, the majority of the reported MOFs are generally in the form of bulk particles, which greatly limits the exposure of active sites. Given this, 2D MOF materials could serve as a promising solution due to their highly exposed architecture, but their complex and time-consuming synthesis processes, generally involving the exfoliation of laminar bulk MOFs, solvothermal growth, or surfactant-assisted preparation, *etc.*, are seriously impeding their large-scale production and wide application.^{27,28}

Here, we developed a facile and fast bottom-up preparation of a unique flower-like zinc–hexamethylenetetramine (ZnHMT) coordination complex for the construction of a multifunctional interlayer in Li–S batteries. Through synthetic optimization,

^aDepartment of Chemical Engineering, Waterloo Institute for Nanotechnology, University of Waterloo, Waterloo, Ontario N2L3G1, Canada. E-mail: aipingyu@uwaterloo.ca; zhwenchen@uwaterloo.ca

^bCollege of Chemistry, Chemical Engineering and Materials Science, Shandong Normal University, Jinan 250014, P. R. China

† Electronic supplementary information (ESI) available. See DOI: 10.1039/c9ta12573f

‡ These authors contributed equally to this work.

uniform ZnHMT microflowers were yielded *via* the self-assembly of ultrathin 2D nanosheets within a few minutes under ambient conditions. When implemented as an interlayer, the as-developed ZnHMT microflowers demonstrate strong affinity to LiPSs through Lewis acid–base interactions, which effectively confines sulfur species, preventing their penetration through the separator, leading to a significant inhibition of polysulfide shuttling. Moreover, the flower-like architecture not only efficiently exposes the adsorption sites for strengthened sulfur immobilization, but also affords facile electrolyte infiltration with fluent ion transfers, thus contributing to a fast and durable sulfur electrochemistry. Consequently, Li–S batteries based on the ZnHMT interlayer realized excellent cycling stability with a low capacity decay rate of 0.03% per cycle over 1000 cycles, a superb rate performance up to 5C and a high areal capacity of 5.9 mA h cm^{-2} under raised sulfur loading.

The preparation of the ZnHMT microflowers is illustrated in Fig. 1a. The direct mixing of $\text{Zn}(\text{NO}_3)_2$ and HMT in ethanol medium renders self-coordination between the Zn ions and organic ligands to yield a white ZnHMT precipitate. The scanning electron microscopy (SEM) observations reveal the spherical structure and uniform size of around 2–3 μm , as well as the exquisite hierarchical flower-like architecture assembled by a bunch of 2D nanosheets (Fig. 1b and c). The energy-dispersive X-ray spectroscopy (EDX) mapping confirms the existence and uniform distribution of Zn, N and C elements in the product (Fig. 1d). Fig. 1e and f show the transmission electron microscopy (TEM) images of the obtained ZnHMT, which further

confirm the elegant flower-like assembly of wrinkled and ultrathin 2D ZnHMT nanosheets with abundant internal voids. The lateral size of the nanosheets can reach several hundred nanometers, while their thicknesses were around 1 nm as determined by atomic force microscope (AFM) measurement (Fig. 1g). Such an ultrathin 2D nano-structure is expected to efficiently expose the active sites, while the flower-like assembly with considerable porosity favors electrolyte infiltration and ion transfer.

The crystalline structure of ZnHMT was investigated by X-ray diffraction (XRD). As shown in Fig. 2a, the characteristic peaks for pure HMT completely vanish in the ZnHMT pattern, accompanied by the emergence of many new peaks, implying the formation of a zinc–hexamethylenetetramine coordination complex.²⁹ This result confirms the successful coordination and the decent crystallinity of the obtained framework. Accordingly, the Fourier transform infrared spectroscopy (FTIR) spectra display broadened and intensified peaks from HMT to ZnHMT at ~ 3463.5 and $\sim 1371.1 \text{ cm}^{-1}$, which can be ascribed to the stretching vibration of O–H and N–O, respectively, indicating the incorporation of hydrophilic nitrate in the product framework (Fig. 2b).³⁰ Meanwhile, the peak splitting at ~ 1238.1 and $\sim 1006.7 \text{ cm}^{-1}$ assigned to the C–N vibration suggests that the networking occurred at N sites through monodentate coordination.^{31,32} Additionally, the porous characters of the obtained ZnHMT microflowers were studied by N_2 adsorption–desorption measurement. The isotherm shows a typical type-II curve, presenting the co-existence of micro- and mesoporous

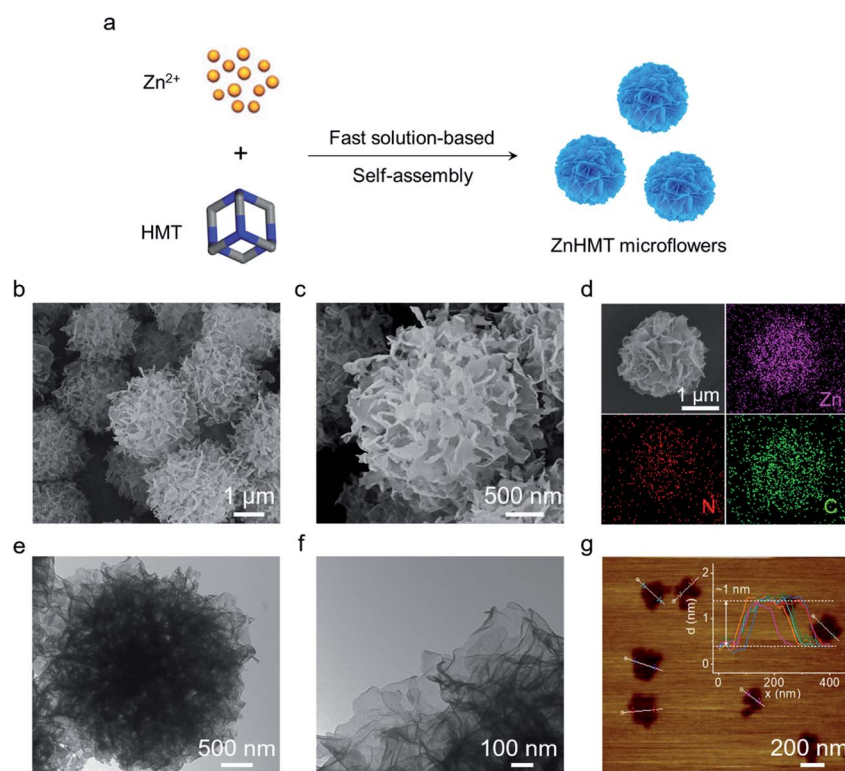


Fig. 1 (a) Schematic illustration of the synthesis of ZnHMT microflowers; (b and c) SEM images, (d) EDX mapping and (e and f) TEM images of the ZnHMT microflowers; (g) AFM image and the thickness of the ZnHMT nanosheets.

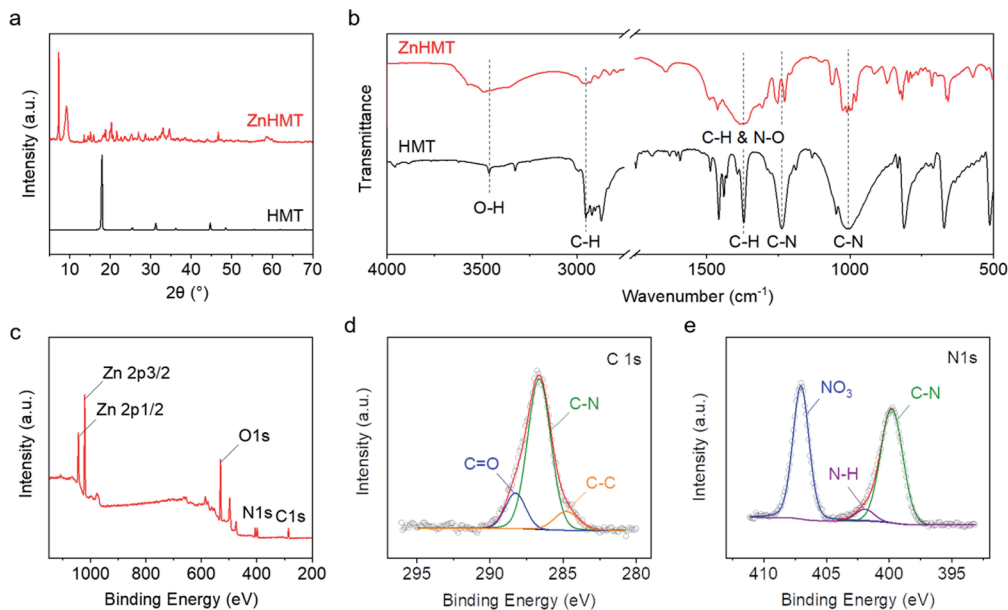


Fig. 2 (a) XRD patterns and (b) FTIR spectra of HMT and ZnHMT; (c) XPS survey, (d) C 1s and (e) N 1s spectra of ZnHMT.

structures with a surface area of $16.1 \text{ m}^2 \text{ g}^{-1}$ (Fig. S1a[†]). The pore size distribution in Fig. S1b[†] reveals the concentrated micropores at around 1.4 nm as well as the broad mesopore distribution at an expanded range over 100 nm. Such a porous and highly-exposed architecture could benefit the contact between ZnHMT and LiPSs for sufficient sulfur immobilization. Furthermore, X-ray photoelectron spectroscopy (XPS) was conducted to analyze the surface chemistry of ZnHMT. The XPS survey spectrum confirms the chemical composition by showing the characteristic peaks of C, N, O and Zn elements, as shown in Fig. 2c. The high-resolution C 1s spectrum can be deconvoluted into three sub-peaks at 284.8, 286.5 and 287.8 eV, corresponding to C–C, C–N and C=O bonding, respectively. The C–C and C=O species can be ascribed to the adventitious carbon contamination, while the dominant C–N peak is consistent with the sole N–CH₂–N structure in HMT (Fig. 2d).^{33–35} Meanwhile, three sub peaks can be differentiated in the N 1s spectrum, as shown in Fig. 2e. The peaks located at 399.8 and 402.0 eV refer to the C–N and N–H bonds, respectively, in HMT, while the peak at 407.0 eV can be assigned to the NO₃[−] species incorporated in the complex framework.^{33,36} It should be noted that despite the successful coordination between ZnNO₃ and HMT, the exact molecular structure of the ZnHMT complex is still vague and requires further investigation (Fig. S2[†]).^{37,38}

In view of the delicate architecture, various synthetical parameters, including reactant molar ratio, temperature, reaction time and water content in the solvent, were systematically investigated to study their impact on the final products. Fig. S3[†] shows the SEM images of ZnHMT obtained at varied Zn to HMT molar ratios from 1 : 1 to 4 : 1. It can be observed that the uniform microflower morphology is only achievable at the ratio of 2 : 1. A lower ratio may result in insufficient bridges for the coordination, while a higher ratio leads to excessively large

nanosheets that fail to undergo spherical self-assembly. Meanwhile, the favorable structure can be reproduced under ambient temperatures (20–30 °C). The spherical morphology is still accessible at lower temperatures, in spite of the relatively messier assembly and the larger sphere size, while an excessively high temperature results in the deconstruction of the self-assembly (Fig. S4[†]). Comparatively, the reaction time imposes little impact on the product morphology as depicted in Fig. S5[†], where uniform microflowers are achievable within 5 min. However, the product is highly sensitive to the water content in the reaction solvent. Moisture at as little as 1% in ethanol is capable of completely destroying the self-assembly structure, while a water content higher than 10% leads to the transformation of the nanosheets into rigid and thick pellets (Fig. S6[†]). Overall, this method enables the facile and fast production of exquisite ZnHMT microflowers with good application prospects.

The interactions between the interlayer materials and LiPSs play vital roles in shuttle regulation. Given this, the interactive chemistry between ZnHMT and LiPSs was firstly verified by the optical polysulfide adsorption (Fig. 3a, inset). It can be clearly observed that the color of the LiPS solution significantly faded after being adsorbed by ZnHMT (Li₂S₆@ZnHMT), visually illustrating the great LiPS adsorbability of the ZnHMT microflowers. Accordingly, the ultraviolet-visible (UV-vis) spectra of the supernatants display drastically weakened LiPS absorbance at around 343 and 413 nm after adsorption by ZnHMT (Fig. 3a),³⁹ further evidencing the greatly reduced LiPS concentration, consistent with the above color change. Beyond that, XPS was carried out to further analyze the interaction mechanism between ZnHMT and Li₂S₆. As shown in Fig. 3b, the S 2p spectrum of pure Li₂S₆ presents two typical peak pairs at 161.3 eV and 162.9 eV, referring to the terminal sulfur (S_T^{−1}) and bridging sulfur (SB0), respectively.⁴⁰ However, these peaks

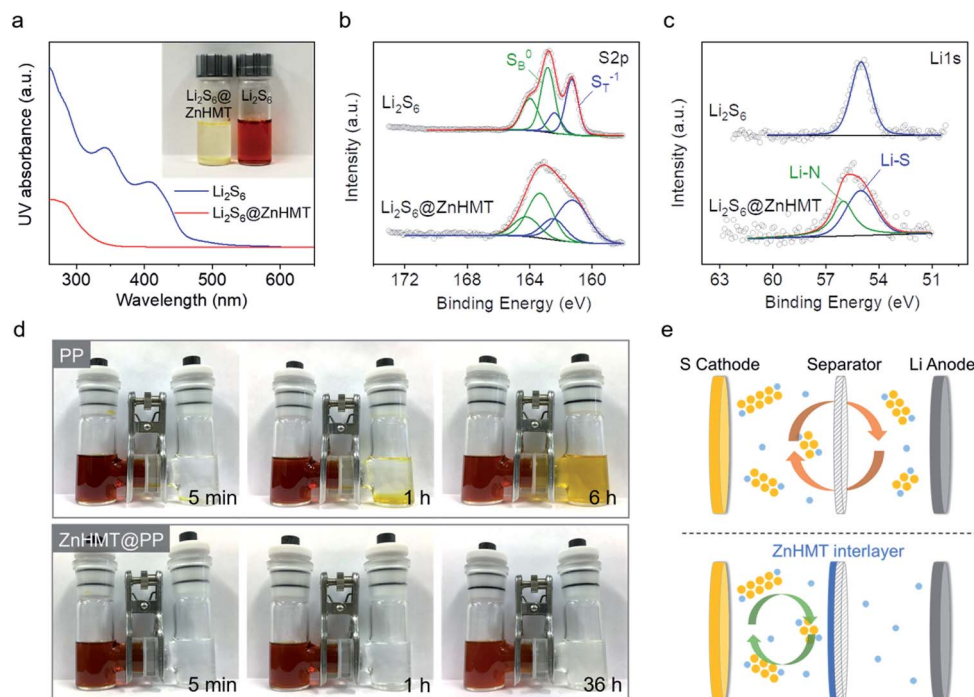


Fig. 3 (a) Optical image of LiPS adsorption by ZnHMT and the corresponding UV-vis spectra; (b) S 2p and (c) Li 1s XPS spectra of LiPSs before and after adsorption by ZnHMT; (d) LiPS diffusion in H-type cells with PP and ZnHMT@PP separators; (e) schematic diagram of shuttle inhibition by the ZnHMT interlayer.

shift to a higher binding energy range in the Li_2S_6 @ZnHMT spectrum, suggesting decreased electron density in the sulfur through the Lewis acid–base interactions between LiPSs and ZnHMT. Meanwhile, the Li 1s spectrum of Li_2S_6 @ZnHMT presents a new peak at 56.0 eV in addition to the Li–S peak (55.0 eV) attributed to the formation of a “lithium bond” (Fig. 3c).⁴¹ In addition, the N 1s and Zn 2p spectra in HMT also undergo significant peak shifts as shown in Fig. S7,[†] further confirming the strong chemical interactions between LiPSs and ZnHMT.

Based on the above results, two factors can be concluded to synergistically contribute to the strong LiPS adsorbability of ZnHMT microflowers, *i.e.*, (i) the high content of Zn and N sites in ZnHMT imposes robust and massive chemical interplay with LiPSs; (ii) the highly-exposed flower-like architecture enables abundant contact with LiPS species and further intensifies the overall adsorption effect. Given this, a ZnHMT-based interlayer was fabricated through a simple slurry-coating technique on a conventional polypropylene (PP)-based membrane (denoted as ZnHMT@PP, see experimental details in the ESI[†]). Super P (SP) was applied as a conductive agent for the reutilization of the trapped LiPSs. Fig. S8[†] shows the homogeneous ZnHMT coating on one side of a PP membrane. The considerably smaller contact angle of an electrolyte drop on the ZnHMT@PP surface than on a pristine PP membrane (22.5° vs. 50.3°) suggests improved electrolyte infiltration by the ZnHMT coating (Fig. S9[†]). The LiPS interception effects of different separators were examined by the LiPS permeation in H-type cells. As displayed in Fig. 3d, the PP-based cell undergoes fast LiPS leaching within 5 min, which further turns the solution to deep yellow

after merely 6 h, signifying the serious LiPS penetration. In contrast, the modified ZnHMT@PP separator enables a well-maintained colorless solution in the opposite chamber even after 36 hours, intuitively indicating its great capability of restraining the LiPS diffusion across the separator. Such LiPS obstruction is expected to effectively confine the active species within the cathode and suppress the shuttle effect for enhanced sulfur utilization, as well as simultaneously protecting the Li anode from detrimental attacks by LiPSs for stabilized sulfur electrochemistry as illustrated in Fig. 3e.

To evaluate the ZnHMT-based interlayer in Li–S batteries, CR2016 coin cells were fabricated with pristine and modified separators. A simple sulfur/super P composite ($\text{S}@\text{SP}$ with S content of 68.8 wt%, Fig. S10[†]) electrode was employed for the evaluations. Fig. 4a shows the typical cyclic voltammetry (CV) curves of cells with different separators at a scanning rate of 0.1 mV s^{-1} . Two characteristic peaks at 2.3 and 2.05 V (vs. Li/Li^+ , hereafter inclusive) can be observed during the cathodic scanning, corresponding to the electrochemical reduction of elemental sulfur into long-chain polysulfides (Li_2S_x , $x = 4-8$), and further reduction into insoluble $\text{Li}_2\text{S}_2/\text{Li}_2\text{S}$, respectively. Accordingly, the strong overlapped peak at 2.35 V refers to the sulfur oxidization back to elemental sulfur upon anodic scanning. It can be noted that the ZnHMT@PP cell exhibits significantly sharper peak shapes with higher current responses, as well as a smaller potential gap of the redox peaks compared with those for the PP cell, suggesting its faster reaction kinetics. The galvanostatic charge–discharge profiles agree well with the CV curves by showing typically two discharge plateaus and one

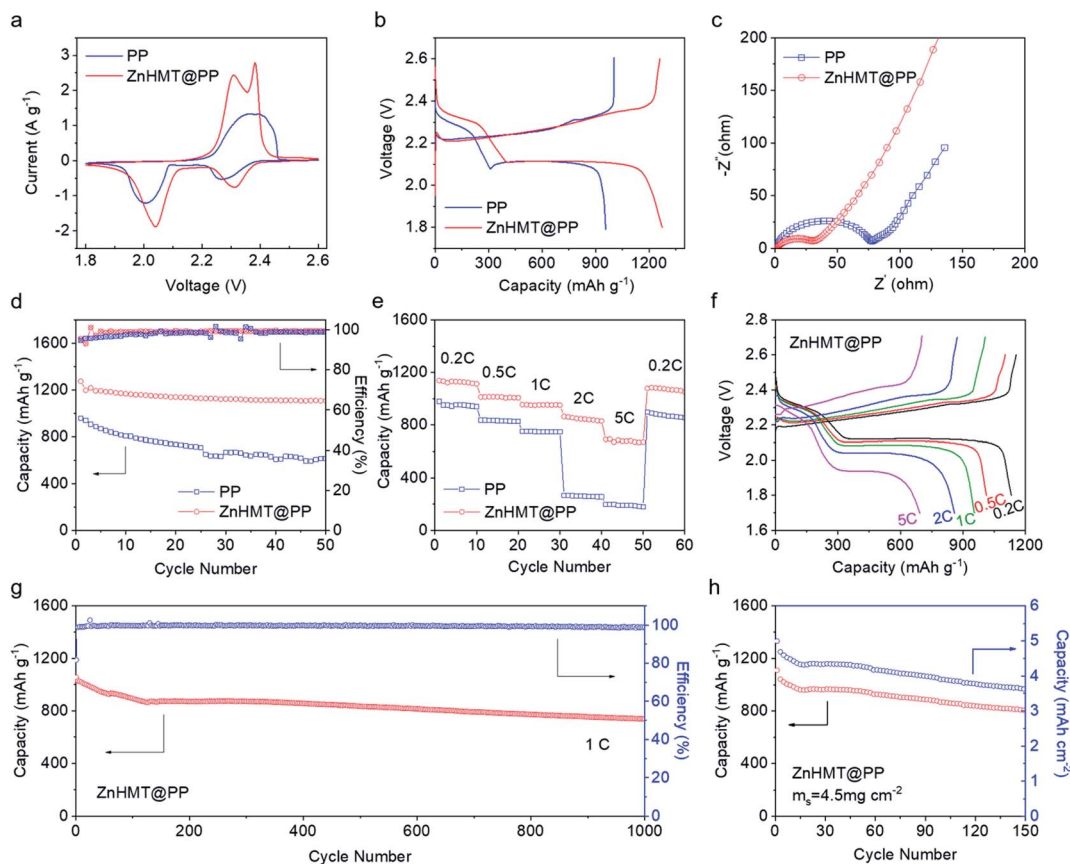


Fig. 4 (a) CV curves, (b) charge–discharge profiles at 0.2C, (c) EIS spectra, (d) cycling performances at 0.2C and (e) multi-rate cycling performances of cells with PP and ZnHMT@PP separators; (f) voltage profiles of the ZnHMT@PP cell under varied current rates; (g) long-term cycling performance of the ZnHMT@PP cell at 1C; (h) cycling performance of the ZnHMT@PP cell at 0.1C under a raised sulfur loading of 4.5 mg cm^{-2} .

long slope upon charging (Fig. 4b). The ZnHMT@PP cell enables a much higher initial capacity of $1273.8 \text{ mA h g}^{-1}$ than that of the PP cell ($956.8 \text{ mA h g}^{-1}$), indicating the greatly enhanced sulfur utilization. Electrochemical impedance spectroscopy (EIS) results show a significantly smaller semicircle for the ZnHMT@PP cell compared with that for the PP cell in the high-medium frequency range (Fig. 4c), indicating the facilitated electron/ion transfer and fast redox reaction in agreement with the CV and voltage profiles.⁴²

Fig. 4d shows the cycling performances of different cells. In comparison, the ZnHMT@PP cell retains a much higher capacity of $1106.9 \text{ mA h g}^{-1}$ (86.9% of its initial value) than the PP cell ($694.1 \text{ mA h g}^{-1}$ and 70.5%) after 50 cycles at 0.2C. Meanwhile, higher and steadier coulombic efficiency can be also maintained for the ZnHMT@PP cell, suggesting the suppressed shuttle effect, enhanced sulfur utilization and improved reaction reversibility attributed to the effective LiPS blocking by the ZnHMT interlayer. The rate capabilities were explored by multi-rate cycling as shown in Fig. 4e. A high capacity of $692.9 \text{ mA h g}^{-1}$ can be sustained at a high rate up to 5C for the ZnHMT@PP cell, whereas the PP-based counterpart undergoes serious capacity decay under raised current rates. This result strongly demonstrates the greatly improved sulfur

reaction kinetics in the ZnHMT-based configuration, which can be also perceived from the corresponding voltage profiles. As shown in Fig. 4f and S11,† the ZnHMT@PP cell well maintains the two-plateau discharge profile even under a high rate of 5C, while the PP cell is only accessible to the one-plateau profile at high rates ascribed to severe electrochemical polarization. Additionally, in view of the different roles of ZnHMT and SP in the composite interlayer, varied ZnHMT to SP ratios were also investigated as shown in Fig. S12.† The results demonstrate a modest ZnHMT to SP ratio of 1 : 1 to balance the conductivity and LiPS adsorbability, which is employed in further characterizations.

To further understand the improvement mechanism of the as-developed ZnHMT-based interlayer for the Li–S battery chemistry, the cycling performance was studied using electrolyte without LiNO_3 additive, which is a well-recognized indicator of the shuttling severity in the corresponding configurations.⁴³ As shown in Fig. S13,† the PP cell exhibits excessively high charge capacities with clear shuttle plateaus at around 2.35 V, corresponding to a serious coulombic inefficiency. By contrast, the cell equipped with the ZnHMT interlayer delivers significantly enhanced coulombic efficiency as well as stabilized capacity, demonstrating an effectively inhibited shuttling

behavior. Such superiorities can be further verified by the self-discharge evaluation performed by recharging the cells to a high voltage and resting for 24 h Fig. 5a shows the self-discharge profiles of different cells. It can be observed that the PP cell undergoes a drastic voltage decline after the open-circuit-voltage (OCV) process, with continuous fading to 2.30 V at the end of the rest period. Distinctly, the ZnHMT@PP cell maintains a constantly higher OCV of 2.38 V after 24 h. The improvement in self-discharge behavior can be also perceived from the voltage profiles before and after the OCV rest period. As shown in Fig. 5b and c, the ZnHMT interlayer enables a well-maintained charge–discharge profile after the OCV rest period, in contrast to the severe voltage and capacity losses in the PP cell. Beyond that, post-cycling characterizations were conducted to further investigate the shuttle inhibition. Fig. 5d and e show the anodic surfaces of different separators. A considerable number of micrometric particles can be observed on the PP membrane, while the ZnHMT@PP separator maintains a relatively clean surface. These particles could be ascribed to the precipitation of insoluble sulfur species derived from the disproportionation and decomposition of LiPSs, which penetrate the separator into the anode section. This deduction can be supported by the significantly higher EDX S signal on the anodic side of the PP separator compared with that of ZnHMT@PP as shown in Fig. 5f, which further verifies the

limited LiPS penetration in ZnHMT@PP cells. Accordingly, the cycled Li surface morphology was also examined (Fig. 5g–i). Compared with the fresh Li, the ZnHMT@PP separator contributes to a well-retained smooth Li surface, while the conspicuous island-like Li surface in the PP cell reflects the inhomogeneous Li-plating aroused by the serious shuttle effect. Additionally, a postmortem ICP test verifies negligible Zn leaching (<0.08%) in the cycled electrolyte, while the TEM observation reveals a well-maintained flower-like architecture (Fig. S14[†]) after cycling, indicating the good structural stability of ZnHMT upon cell operation. All of these results consistently evidence the highly effective shuttle inhibition by the as-developed ZnHMT interlayer, which establishes a reliable barrier against LiPS penetration and confines the active species within the cathode for enhanced sulfur utilization and stabilized sulfur redox reactions.

On this basis, a long-term evaluation was further performed to probe the cyclability of the ZnHMT@PP cell as shown in Fig. 4g. A high capacity of 738.6 mA h g⁻¹ can be achieved after 1000 cycles at 1C, corresponding to a favorable capacity retention of 70% and an ultralow capacity fading rate of 0.03% per cycle. Meanwhile, a high coulombic efficiency close to unity can be well sustained upon cycling, demonstrating excellent electrochemical reversibility. This result further highlights the reliable sulfur electrochemistry through the construction of the

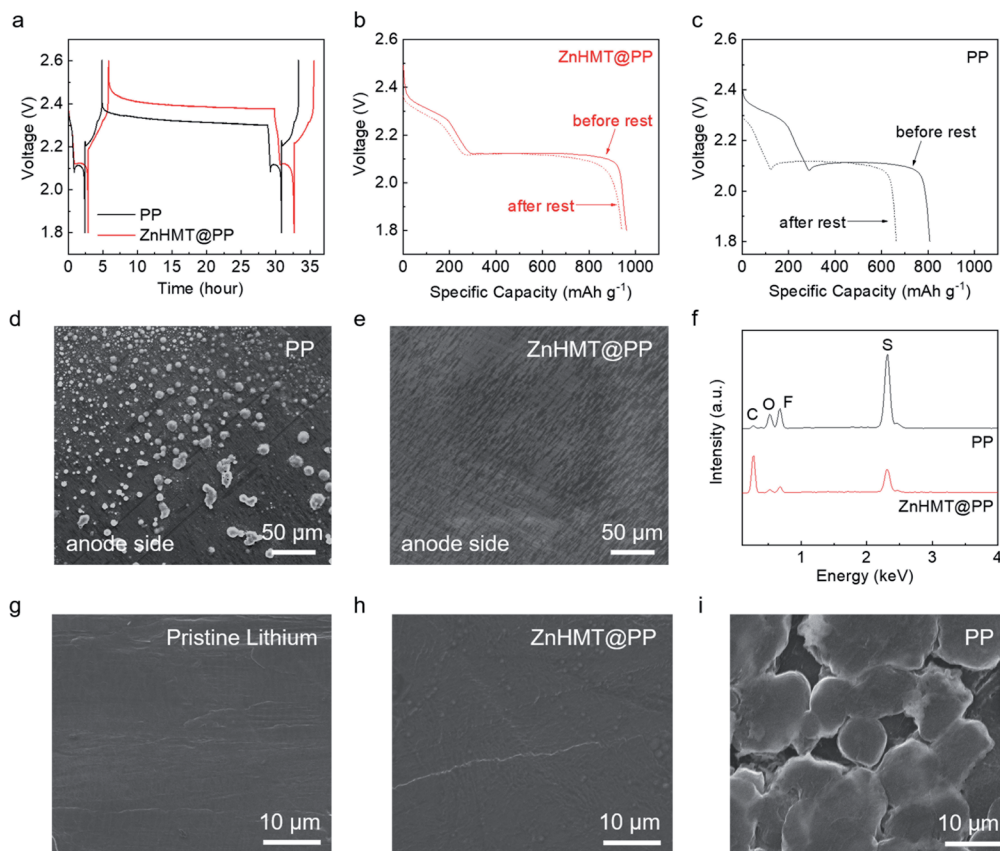


Fig. 5 (a) Self-discharge profiles of cells with PP and ZnHMT@PP; discharge profiles of (b) ZnHMT@PP and (c) PP cells before and after the OCV rest period; (d and e) surface morphologies and (f) EDX spectra of PP and ZnHMT@PP separators facing the anodes after cycling; surface morphologies of Li foils in (g) the fresh state and cycled in cells with (h) ZnHMT@PP and (i) PP separators.

ZnHMT interlayer. Beyond that, the cell performance under raised sulfur loading was explored toward higher energy density. As shown in Fig. S15,† a continuous increase of the areal capacity can be achieved along with the increase of the sulfur loading from 1.2 to 5.7 mg cm⁻², rendering a considerably high areal capacity of up to 5.9 mA h cm⁻². Moreover, cycling evaluation was further conducted for the ZnHMT@PP cell under a high sulfur loading of 4.5 mg cm⁻², which retains a high areal capacity of 3.64 mA h cm⁻² even after 150 cycles, attributed to the facilitated and stabilized sulfur electrochemistry by the ZnHMT interlayer (Fig. 4h), demonstrating good prospects in developing high-performance and practically viable Li-S batteries.

Conclusions

In summary, facile and fast production of hierarchical ZnHMT microflowers was realized through the solution-based self-assembly of ultrathin 2D nanosheets, which was employed for the construction of a multifunctional interlayer for improved Li-S battery performance. The unique flower-like architecture not only facilitates the electrolyte infiltration for expediting ion transfer, but also efficiently exposes active sites for sulfur immobilization. Moreover, the chemical interactions between ZnHMT and LiPSs empowers a strong LiPS adsorbability against their shuttling behavior. Attributed to these superiorities, the ZnHMT-based interlayer establishes a reliable LiPS barrier that effectively obstructs the LiPS diffusion across the separator and confines the active species within the cathode, leading to excellent shuttle inhibition and stable sulfur electrochemistry. As a result, Li-S cells based on the ZnHMT-modified separator achieved an outstanding cycling stability over 1000 cycles, favorable rate capability up to 5C, and a decent areal capacity of 5.9 mA h cm⁻² under raised sulfur loading. This work not only paves a facile pathway toward high-performance Li-S batteries, but also holds considerable instructive and applicable significance for material designs in other related energy storage and conversion fields.

Conflicts of interest

There are no conflicts to declare.

Acknowledgements

The authors acknowledge the support from the Natural Sciences and Engineering Research Council of Canada, University of Waterloo and Waterloo Institute for Nanotechnology.

Notes and references

- 1 M. Armand and J. M. Tarascon, *Nature*, 2008, **451**, 652.
- 2 Z. P. Cano, D. Banham, S. Y. Ye, A. Hintennach, J. Lu, M. Fowler and Z. W. Chen, *Nat. Energy*, 2018, **3**, 279.
- 3 P. G. Bruce, S. A. Freunberger, L. J. Hardwick and J. M. Tarascon, *Nat. Mater.*, 2011, **11**, 19.
- 4 A. M. Haregewoin, A. S. Wotango and B. J. Hwang, *Energy Environ. Sci.*, 2016, **9**, 1955.
- 5 G. R. Li, Z. W. Chen and J. Lu, *Chem*, 2018, **4**, 3.
- 6 A. Manthiram, Y. Z. Fu, S. H. Chung, C. X. Zu and Y. S. Su, *Chem. Rev.*, 2014, **114**, 11751.
- 7 G. R. Li, S. Wang, Y. N. Zhang, M. Li, Z. W. Chen and J. Lu, *Adv. Mater.*, 2018, **30**, 1705590.
- 8 Y. X. Yin, S. Xin, Y. G. Guo and L. J. Wan, *Angew. Chem., Int. Ed. Engl.*, 2013, **52**, 13186.
- 9 G. Y. Xu, B. Ding, J. Pan, P. Nie, L. F. Shen and X. G. Zhang, *J. Mater. Chem. A*, 2014, **2**, 12662.
- 10 C. B. Bucur, J. Muldoon and A. Lita, *Energy Environ. Sci.*, 2016, **9**, 992.
- 11 M. Wild, L. O'Neill, T. Zhang, R. Purkayastha, G. Minton, M. Marinescu and G. J. Offer, *Energy Environ. Sci.*, 2015, **8**, 3477.
- 12 H. J. Peng, J. Q. Huang, X. B. Cheng and Q. Zhang, *Adv. Energy Mater.*, 2017, **7**, 1700260.
- 13 Y. K. Wang, R. F. Zhang, J. Chen, H. Wu, S. Y. Lu, K. Wang, H. L. Li, C. J. Harris, K. Xi, R. V. Kumar and S. J. Ding, *Adv. Energy Mater.*, 2019, **9**, 1900953.
- 14 L. L. Fan, M. Li, X. F. Li, W. Xiao, Z. W. Chen and J. Lu, *Joule*, 2019, **3**, 361.
- 15 Y. Yang, G. Y. Zheng and Y. Cui, *Chem. Soc. Rev.*, 2013, **42**, 3018.
- 16 G. Li, W. Lei, D. Luo, Y. Deng, Z. Deng, D. Wang, A. Yu and Z. Chen, *Energy Environ. Sci.*, 2018, **11**, 2372.
- 17 S. Rehman, K. Khan, Y. F. Zhao and Y. L. Hou, *J. Mater. Chem. A*, 2017, **5**, 3014.
- 18 Y. S. Su and A. Manthiram, *Nat. Commun.*, 2012, **3**, 1166.
- 19 T. H. Zhou, W. Lv, J. Li, G. M. Zhou, Y. Zhao, S. X. Fan, B. L. Liu, B. H. Li, F. Y. Kang and Q. H. Yang, *Energy Environ. Sci.*, 2017, **10**, 1694.
- 20 W. L. Cai, G. R. Li, K. L. Zhang, G. N. Xiao, C. Wang, K. F. Ye, Z. W. Chen, Y. C. Zhu and Y. T. Qian, *Adv. Funct. Mater.*, 2018, **28**, 1704865.
- 21 J. Q. Huang, Q. Zhang and F. Wei, *Energy Storage Materials*, 2015, **1**, 127.
- 22 Y. B. He, Z. Chang, S. C. Wu and H. S. Zhou, *J. Mater. Chem. A*, 2018, **6**, 6155.
- 23 H. Furukawa, K. E. Cordova, M. O'Keeffe and O. M. Yaghi, *Science*, 2013, **341**, 974.
- 24 J. Lee, O. K. Farha, J. Roberts, K. A. Scheidt, S. T. Nguyen and J. T. Hupp, *Chem. Soc. Rev.*, 2009, **38**, 1450.
- 25 Y. Zheng, S. S. Zheng, H. G. Xue and H. Pang, *J. Mater. Chem. A*, 2019, **7**, 3469.
- 26 Y. Mao, G. Li, Y. Guo, Z. Li, C. Liang, X. Peng and Z. Lin, *Nat. Commun.*, 2017, **8**, 14628.
- 27 M. T. Zhao, Y. Huang, Y. W. Peng, Z. Q. Huang, Q. L. Ma and H. Zhang, *Chem. Soc. Rev.*, 2018, **47**, 6267.
- 28 S. Furukawa, J. Reboul, S. Diring, K. Sumida and S. Kitagawa, *Chem. Soc. Rev.*, 2014, **43**, 5700.
- 29 S. T. Liu, J. S. Zhou and H. H. Song, *Adv. Energy Mater.*, 2018, **8**, 1800569.
- 30 R. Kruszynski, T. Sieranski, M. Swiatkowski, M. Zielak, J. Wojciechowski, M. Dzierzawska and B. Lewinski, *J. Coord. Chem.*, 2014, **67**, 1332.

- 31 C. D. Tabong, A. M. Ondoh, D. M. Yufanyi and J. Foba, *J. Mater. Sci.*, 2015, **4**, 70.
- 32 E. G. Palacios, G. Juarez-Lopez and A. J. Monhemius, *Hydrometallurgy*, 2004, **72**, 139.
- 33 Y. Wang, P. Zhang, C. Y. Ye, W. S. Fu, H. Yuan, P. P. Hu and Y. Liu, *New J. Chem.*, 2018, **42**, 3519.
- 34 T. L. Barr and S. Seal, *J. Vac. Sci. Technol., A*, 1995, **13**, 1239.
- 35 G. Greczynski and L. Hultman, *Prog. Mater. Sci.*, 2020, **107**, 100591.
- 36 C. E. Nanayakkara, P. M. Jayaweera, G. Rubasinghege, J. Baltrusaitis and V. H. Grassian, *J. Phys. Chem. A*, 2014, **118**, 158.
- 37 K. H. Jia and S. H. Ba, *Johnson Matthey Technol. Rev.*, 2018, **62**, 89.
- 38 G. Singh, B. P. Baranwal, I. P. S. Kapoor, D. Kumar, C. P. Singh and R. Frohlich, *J. Therm. Anal. Calorim.*, 2008, **91**, 971.
- 39 G. R. Li, W. Lei, D. Luo, Y. P. Deng, D. L. Wang and Z. W. Chen, *Adv. Energy Mater.*, 2018, **8**, 1702381.
- 40 X. Liang, C. Hart, Q. Pang, A. Garsuch, T. Weiss and L. F. Nazar, *Nat. Commun.*, 2015, **6**, 5682.
- 41 T. Z. Hou, W. T. Xu, X. Chen, H. J. Peng, J. Q. Huang and Q. Zhang, *Angew. Chem., Int. Ed.*, 2017, **56**, 8178.
- 42 Z. F. Deng, Z. A. Zhang, Y. Q. Lai, J. Liu, J. Li and Y. X. Liu, *J. Electrochem. Soc.*, 2013, **160**, A553.
- 43 G. R. Li, C. Wang, W. L. Cai, Z. Lin, Z. P. Li and S. Q. Zhang, *NPG Asia Mater.*, 2016, **8**, e317.